Transport studies in 2D transition metal dichalcogenides and black phosphorus

2016 J. Phys.: Condens. Matter 28 263002

(http://iopscience.iop.org/0953-8984/28/26/263002)

IOP Publishing Journal of Physics: Condensed Matter
J. Phys.: Condens. Matter **28** (2016) 263002 (13pp) doi:10.1088/0953-8984/28/26/263002

Topical Review

Transport studies in 2D transition metal dichalcogenides and black phosphorus

Yuchen Du, Adam T Neal, Hong Zhou and Peide D Ye

School of Electrical and Computer Engineering and Birck Nanotechnology Center, Purdue University, West Lafayette, IN 47907, USA

E-mail: yep@purdue.edu

Received 20 February 2015, revised 8 April 2016
Accepted for publication 11 April 2016
Published 17 May 2016

Abstract

Two-dimensional (2D) materials are a new family of materials with interesting physical properties, ranging from insulating hexagonal boron nitride, semiconducting or semi-metallic transition metal dichalcogenides, to gapless metallic graphene. In this review, we provide a brief discussion of transport studies in transition metal dichalcogenides, including both semiconducting and semi-metallic phases, as well as a discussion of the newly emerged narrow bandgap layered material, black phosphorus, in terms of its electrical and quantum transport properties at room and cryogenic temperatures. Ultra-thin layered channel materials with atomic layer thickness in the cross-plane direction, together with relatively high carrier mobility with appropriate passivation techniques, provide the promise for new scientific discoveries and broad device applications.

Keywords: TMDs, black phosphorus, phosphorene, 2D materials

(Some figures may appear in colour only in the online journal)

1. Introduction

The discovery of graphene has been important not only to demonstrate the existence of thermodynamically stable two-dimensional (2D) crystals, but also to introduce a family of materials with extremely high crystal quality, new physical phenomena, and unique properties [1–4]. The most exceptional electronic quality in graphene is that charge carriers can travel thousands of interatomic distances without scattering. With this inherent advantage, the mobility of graphene has been observed to approach 15 000 $cm^2\ V^{-1}\ s^{-1}$ in ambient atmosphere, and can exceed 100 000 $cm^2\ V^{-1}\ s^{-1}$ at low temperatures [5–10]. Graphene's transport properties also stand out as it shows a pronounced ambipolar behavior, where the charge carrier behavior in graphene can be tuned continuously between that of electrons or holes by applying an external electric field [3, 7, 8]. With such benefits, the rise of graphene with one single atomic layer thickness in the cross-plane direction, easily exfoliated due to the layer-to-layer van der Waals interaction, offers many new inroads into low-dimensional physics. One aspect of graphene that severely limits its potential for electronic applications is its lack of a bandgap and the resulting large off-state current during transistor operation [7, 10]. Various functionalized forms of graphene can be generated and accompanied with certain values of energy gap, but, this comes at severe cost to its transport properties, resulting in degraded carrier mobility [11–13]. As a potential alternative, gapped semiconducting transition metal dichalcogenides (TMDs) have been introduced into 2D materials research in recent years. The TMD family is composed of strong *X*–*M*–*X* intralayer covalent bondings, where *M* indicates a transition metal group material, and *X* represents chalcogen atoms (either Se, S, or Te) [14, 15]. This family of new materials has been regarded as a promising candidate for field-effect transistors (FETs) with relatively high on/off ratios and reasonable carrier mobility [16–24]. In addition to TMDs, it is interesting to explore other new 2D semiconductors with much higher carrier mobility. Black phosphorus (BP) is one

of the promising candidates, which has a narrow bandgap of 0.3 eV in bulk form. As this material is thinned down to the monolayer limit, which has been termed phosphorene, the bandgap varies as a function of the number of layers, going up to 2.0 eV in the monolayer [25–27]. The history of bulk BP can be traced back to a century ago. It was first synthesized from red phosphorus under high temperature and pressure [28]. In the past century, the synthesis, physical properties, and device applications of bulk BP have been investigated to some extent. The successful exfoliation of monolayer phosphorene, leading to the discovery of superior transport properties of the ultra-thin BP film, has generated wide research interest in this nanomaterial, because BP bridges the gap between zero bandgap graphene and wide bandgap TMDs, thereby providing a brand new avenue to expand the scope of experimentally accessible 2D crystals, and pursue a broad range of transport studies.

2. Transport studies in semiconductor and metallic TMDs

MoS_2, one of the most studied materials from the TMD family, has shown a stable direct excitonic transition energy at the Brillouin zone K point with varied thickness. However, the indirect bandgap in MoS_2 increases monotonically as the number of layers decreases [29, 30]. Under such circumstances, the indirect transition energy becomes so high in monolayer MoS_2 that the material changes into a semiconductor with a direct bandgap of around 1.9 eV [16, 31]. This section centers on the fundamental transport studies of TMDs, which are currently being characterized with weak localization, weak antilocalization, and Hall effect measurements. We also integrate approaches being developed to reach superconductivity in TMDs by applying ionic liquid gating and high pressure methods. Furthermore, we have highlighted key progress in transport studies of MoS_2 through study of an hBN-encapsulated heterostructure, which shows quantum oscillations at low temperatures. Transport studies in TMDs offer abundant opportunities for conducting both fundamental and technologically relevant research, paving the way to generate new device concepts in the future.

2.1. Weak localization effect in MoS_2

An investigation into the magneto-transport properties of MoS_2 starts with characterizing phase coherence length and spin–orbit scattering length via weak localization measurements and Hall effect measurements [32]. The weak localization effect originates from the constructive interference of backscattered electronic wave functions which increases the probability of scattering an electron. This phenomenon manifests itself by a positive correction to resistivity under small magnetic fields. The application of a magnetic field induces an additional phase difference to break the constructive interference, leading to negative magneto-resistance and positive magneto-conductance [33, 34]. The magneto-conductivity is calculated from the measured ρ_{xx} and ρ_{xy} by matrix inversion, and an observed positive magneto-conductivity at zero magnetic field over the studied temperature range of gate voltages is shown in figure 1(a), characteristic of a weak localization effect. To gain insight into the phase coherence length, experimental data curves can be fitted by the Hikami–Larkin–Nagaoka (HLN) model [34]. An estimated phase coherence length as a function of carrier density has been depicted in figure 1(b), in which a magnitude of 50 nm phase coherence length is reported over a back gate bias of 40 V up to 100 V. The weak localization effect also presents a temperature-dependent behavior. The phase coherence length, extracted from the temperature dependent magneto-conductivity curve, decays as $T^{-0.5}$ at two different back gate voltages, which suggests that electron–electron scattering is attributed to the dephasing of the electron wave function [35]. In contrast to silicon, where only inter-valley scattering is important with negligible spin–orbit scattering, or narrow bandgap III–V quantum wells, in which only spin–orbit scattering is important within a single valley, the significance of probing spin and valley properties of MoS_2 stands out as its accommodation of inter-valley scattering and spin–orbit scattering, which are simultaneously present in one single material [32]. MoS_2 and other TMDs have provided a new type of material system with inherent superiority to study the interaction of these scattering mechanisms. As a proof of concept, the fitting parameter extracted from the HLN formula is shown in figure 1(c). The values of the fitting parameter over a range of carrier densities are greater than 0 but less than 2, so that the observed magneto-transport indicates a weak localization phenomenon, but cannot be explained by inter-valley scattering alone. Therefore, further reduction of the fitting parameter below 2 is appointed to spin–orbit scattering, which is strong enough to reduce but weak enough to realize a weak antilocalization. The estimated spin–orbit scattering lengths are shown in figure 1(d). The magnitudes of spin–orbit scattering lengths increase with increasing carrier density, reaching as high as 430 nm at a carrier density of 1.1×10^{13} cm^{-2}.

2.2. Quantum phenomenon in a hBN-encapsulated MoS_2 heterostructure

MoS_2 holds great promise for electrical, optical, and mechanical devices because its relatively large bandgap allows for FETs with a very low off-state current. However, the electron mobility of monolayer and few-layer MoS_2 has so far been found to be substantially below the theoretically predicted limits [36–38]. Beyond mechanical exfoliation, chemical vapor deposition (CVD) has proved to be an effective method for 2D crystal growth to realize large scale syntheses for future manufacturable technology. The earliest attempts to obtain monolayer MoS_2 relied on the solid state sulfurization of molybdenum and molybdenum compounds [39, 40], or the sulfurization of MoO_3 [41, 42]. Typically, these synthetic routes provide a low cost path to achieve high yield and large area thin films, but with the sacrifice of a carrier mobility as low as 0.1–10 cm^2 V^{-1} s^{-1} [20, 39–42]. On the other hand, the room temperature field-effect mobility of exfoliated few-layer MoS_2 onto a SiO_2 substrate reported so far is below 100 cm^2 V^{-1} s^{-1}, which also has hampered efforts

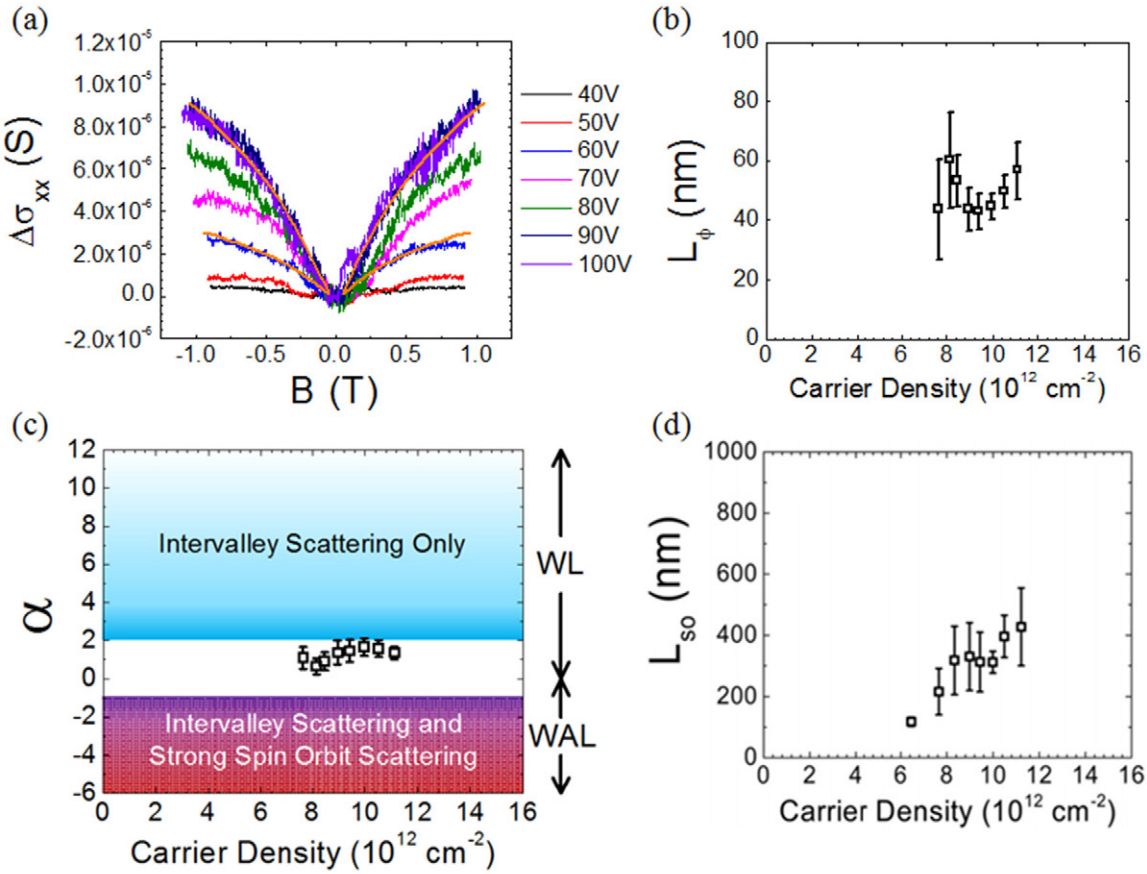

Figure 1. (a) Differential magneto-conductivity curves versus magnetic field of electron-doped few-layer MoS_2 for different applied back gate voltages. (b) Phase coherence length (c) fitting parameter α, and (d) spin–orbit scattering length as a function of carrier density determined by applying the HLN equation. Reproduced with permission from [32]. Copyright 2013 American Chemical Society.

to observe its intrinsic quantum physics in low temperature magneto-transport. Defects such as sulfur vacancies in the MoS_2, charge traps present at the interface between the substrate and the MoS_2 layer, as well as surface scattering from neighboring adsorbates under atmospheric conditions all act as potential sources of disorder and scattering that have been proposed as the dominant cause for such low mobility in MoS_2 [38, 43–46]. In order to reduce extrinsic scattering and improve electron mobility, Cui *et al* have recently developed a van der Waals heterostructure platform wherein MoS_2 layers are fully encapsulated by hexagonal boron nitride (hBN) layers and the device is contacted with gate-tunable graphene electrodes [47]. To examine the quality of the hBN-encapsulated devices, Hall mobility for 1–6 layer samples was derived in figure 2(a) as a function of temperature, with maximum values ranging from 1020 $cm^2\ V^{-1}\ s^{-1}$ in the CVD monolayer to 34 000 $cm^2\ V^{-1}\ s^{-1}$ for a 6-layer MoS_2 device at cryogenic temperatures. The considerably enhanced Hall mobility enabled the observation of the Shubnikov–de Haas (SdH) oscillations for the first time in MoS_2, providing additional strong evidence of the high quality of the hBN-encapsulated MoS_2 sample. Magneto-resistance (R_{xx}) and Hall resistance (R_{xy}) of a 6-layer MoS_2 device as a function of magnetic field at a constant temperature of 0.3 K are shown in figure 2(b). For the 6-layer sample, which has the highest carrier mobility at low temperature, the onset of SdH oscillation roughly occurred at 1 T, and plateau-like oscillation structures begin to unveil in the Hall resistance under the high magnetic field. These emerging features were similar to the early studies of the quantum Hall effect (QHE) on graphene, giving hope that fully developed quantum states, in particular related to spin and valley physics, can be observed with further improvement of sample quality in MoS_2.

2.3. Weak antilocalization effect in metallic 2H-$TaSe_2$

Single crystal heterostructures are typically realized with chemically dissimilar lattice-matched compounds via heteroepitaxy or solid-state reaction. Nevertheless, the family of layered atomically thin TMD materials is unique in that it is chemically homogeneous but exhibits both semiconducting and metallic polymorphs that are lattice matched in principle. For a trigonal prismatic (2H) phase, chalcogen atoms in the upper layer are located directly above those in the lower layer. On the other hand, within octahedral (1T) geometry, chalcogen atoms in the upper and lower planes offset each other, letting transition metal atoms occupy the octahedral holes of chalcogen layers [48, 49]. Certain methods, such as lithium intercalation, would process the phase transition of TMDs from a 2H-semiconductor to 1T-metallic [50–53]. Similar to graphene, although metallic TMDs are not suitable as FET channel materials, they can be engineered as part of

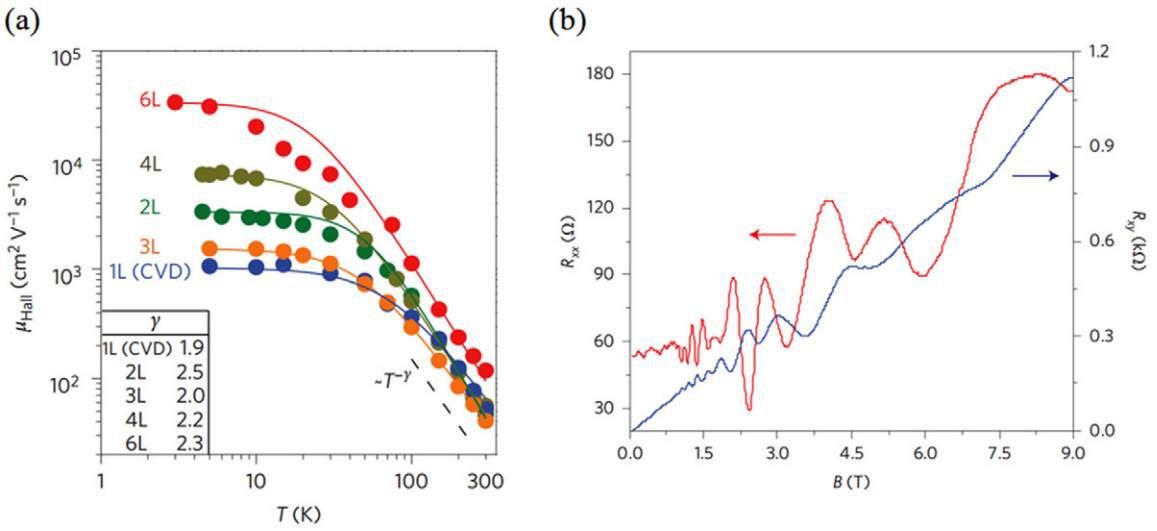

Figure 2. (a) Hall mobility of hBN-encapsulated MoS_2 devices with different numbers of layers of MoS_2 as a function of temperature. (b) Longitudinal resistance R_{xx} (red curve) and Hall resistance R_{xy} (blue curve) of an hBN-encapsulated 6-layer MoS_2 device as a function of magnetic field. The measurement was conducted at 3 K and with a carrier density of 5.3×10^{12} cm^{-2}. Reproduced with permission from [47]. Copyright 2015 Nature Publishing Group.

the contact regions for low resistive contacts [54]. Interest in metallic TMDs is on the rise also in condensed-matter physics because of their superconducting [55, 56] and charge-density wave (CDW) properties [57–59]. Another important application of metallic TMDs, particularly of 2H-$TaSe_2$, is for spintronics devices. Recent work on the magneto-transport of metal in 2H-$TaSe_2$ has characterized a weak antilocalization effect [60], in which a system with spin–orbit coupling denotes that the spin of a carrier is coupled to its momentum. Instead of correcting magneto-conductance with a reduced depth, weak antilocalization shows an enhanced magneto-conductance within a small magnetic field. The strong spin–orbit coupling may make $TaSe_2$ an ideal 2D material for the spin Hall effect [60, 61]. In contrast to the semiconductor phase of MoS_2, which demonstrates a weak localization effect, spin–orbit coupling in 2H-$TaSe_2$ is strong enough to reverse the fitting parameter to achieve a weak antilocalization. Differential magneto-conductivity of 2H-$TaSe_2$ over the studied range of temperatures is depicted in figure 3(a). The negative magneto-conductivity is a standard characteristic of weak antilocalization, and represents a strong spin–orbit coupling phenomenon. As shown in figure 3(b), the average magnitude of the spin–orbit scattering length in 2H-$TaSe_2$ is 17 nm, which is comparable to the spin–orbit scattering length of Pt, indicating a future potential of $TaSe_2$ in 2D spintronics devices. The weak antilocalization effect when the bias current is increased, as shown in figure 3(c), corresponds to a reduced spin–orbit coupling as extra energy is introduced into the system. In addition to strong spin–orbit coupling, a material must also support a large charge current to achieve spin-transfer-torque via the spin Hall effect. Along with this interest, breakdown current density of 2D 2H-$TaSe_2$ has been engineered for the first time to test its ability to conduct DC current. Measurement of the breakdown current density is performed by continuously increasing the bias voltage across the device until a decrease in current of more than 1 order of magnitude is observed. A maximum breakdown current density of 3.7×10^7 A cm^{-2} is observed and presented in figure 3(d) among a total of 18 devices. This large breakdown current density further demonstrates the potential of 2H-$TaSe_2$ as a future spin-torque device.

2.4. Superconductivity in gate-tuned semiconductor TMDs

In recent years, the electrostatic carrier doping technique has been widely utilized by engineering ionic liquids to form an electrical double layer of high capacitance [62–69]. This method has produced carrier densities that span the superconducting dome in high critical temperature (T_c) [70, 71], and proved itself as a practical tool to exhibit superconducting behavior in TMD family materials [72–74]. The key point to achieve a superconducting dome in TMD is to use ionic liquid for electrostatic gating, which can accumulate charge carriers at the surface of the channel material, reaching an order of 10^{14} cm^{-2} density that is significantly greater than conventional high-k dielectrics. So far, only a very limited selection of 2D materials have shown correlated electron states, such as electrostatically induced superconductivity under ionic liquid gating. The effect of the channel material itself is not very clear and is one of the immediate areas requiring further study. Ionic liquid gated TMD superconductivity was reported by Ye *et al* in 2012, in which they observed a superconducting dome in the temperature-carrier density phase diagram of 2H-MoS_2 [72]. Electrostatic carrier doping is achieved through a combination of ionic liquid and solid gating, and a large enhancement in the critical temperature T_c occurs at optimal doping in the chemically inaccessible density regime. A clear phase transition from the insulating state to the superconducting state is realized in gate-tuned band insulator MoS_2 as a result of liquid ionic gate enhancement. Superconductivity emerges at a liquid gate bias of 4 V, and T_c is around 10.5 K. Electrostatically induced density of carriers

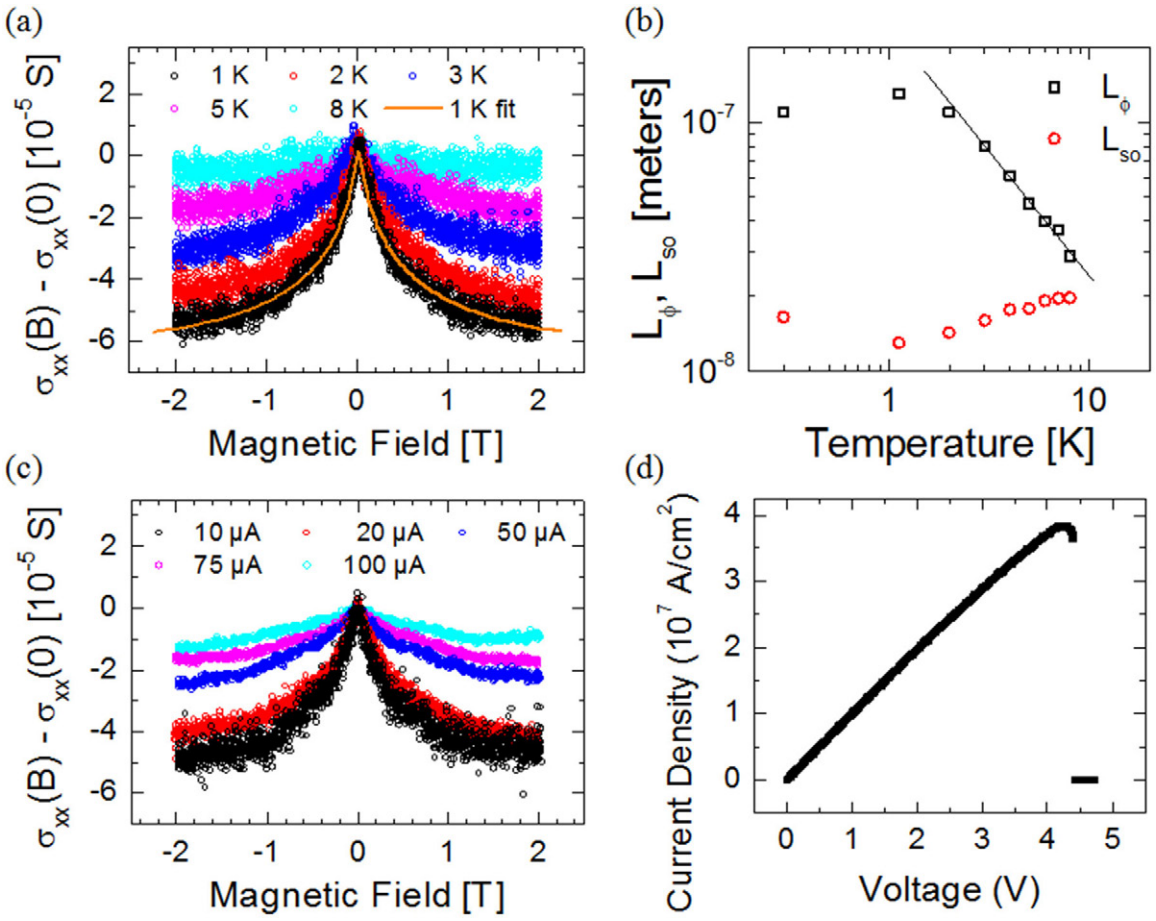

Figure 3. (a) Differential magneto-conductivity curves of 2H-$TaSe_2$ at temperatures from 1 K to 8 K. The negative magneto-conductivity is the characteristic of weak antilocalization and indicates a strong spin–orbit coupling of $TaSe_2$. (b) Phase coherence length L_ϕ (black squares) and spin–orbit scattering length L_{so} (red circles) extracted from the weak antilocalization data as a function of temperature. (c) Differential magneto-conductivity curves of 2H-$TaSe_2$ for different bias currents. (d) DC current density versus voltage characteristic of the $TaSe_2$ device which shows the highest breakdown current. Reproduced with permission from [60]. Copyright 2014 American Chemical Society.

are also calculated, where the phase diagram shows the evolution of different electronic phases as a function of carrier density, ranging from insulating ($n_{2D} < 6.7 \times 10^{12}$ cm^{-2}), and metallic (6.7×10^{12} cm$^{-2} < n_{2D} < 6.8 \times 10^{13}$ cm^{-2}), to superconducting ($n_{2D} > 6.8 \times 10^{13}$ cm^{-2}). Similar work regarding a tungsten-based semiconducting TMD was also published in early 2015 [74]. A detailed characterization as a function of temperature and magnetic field clearly presents the occurrence of a gate-induced superconducting transition below a critical temperature $T_c = 4$ K by investigating transport through ionic liquid gated WS_2 FETs. Overall, compared to WS_2, superconductivity in MoS_2 appears to be much more robust with a significantly higher critical temperature, surviving up to much larger magnetic fields, bearing greater critical current, and exhibiting a considerably narrow width of the superconducting transition as a function of temperature [74]. In addition to the ionic liquid induced electrostatic effect, the application of ultra-high pressure could also dramatically change the material's property, and produce an insulator-to-metal transition [75–79]. Previous work by Chi *et al* has demonstrated that the layered atomic structure of 2H-MoS_2 undergoes a polymorphic structure transition from $2H_c$ to $2H_a$ under high pressure, following a bandgap closing process near 20–30 GPa [78]. Recently, they presented experimental evidence of superconductivity in pristine MoS_2 at ultra-high pressure [80]. The semiconducting states of MoS_2 dominate below 60 GPa, whereas the metallic state prevails between 60 GPa and 90 GPa. Above 90 GPa, the entire system completely transforms into a metallic state, out of which superconductivity evolves, indicated by a precipitous drop in resistance [80]. Meanwhile, the critical temperature enhances from 5 K at 90 GPa to 9 K at 110 GPa, and eventually saturates at 11.5 K over the pressure range of 120 GPa up to 200 GPa. This reported T_c is comparable to the onset temperature of ionic liquid gating. Pressure-induced superconductivity in WTe_2 is also successfully achieved, where the superconducting state first appears at 2.5 GPa. The maximum observed critical temperature is 7 K in an ionic liquid gated WTe_2 superconductor, at the pressure limit of 16.8 GPa [81]. Critical temperatures of selected 2H-TMDs through both ionic liquids and high pressure are summarized in table 1.

The superconducting resistive transition of the layered compound niobium diselenide ($NbSe_2$) had been first observed for crystals a few layer thick in 1972. T_c decreases as the

Table 1. Critical temperatures of selected 2H-TMDs by generating ionic liquids and high pressure methods.

Technique	MoS_2	$MoSe_2$	$MoTe_2$	WS_2	WTe_2
Ionic liquids	10.5 K	7.1 K	X	4.0 K	X
High pressure	11.5 K	X	X	X	7.0 K

crystal thickness is reduced below six $NbSe_2$ layers, and a T_c of 3.8 K was predicted for a single layer [82]. Recently, more detailed studies regarding layer-dependent superconductivity in $NbSe_2$ have been reported without applying ionic liquids or high pressure [83–86]. Bulk $NbSe_2$ behaves as a good metal with a residual resistance ratio exceeding 30 before reaching the superconducting transition at $T_c \sim 7$ K. Similar behavior is observed in atomically thin samples with progressive suppression of T_c to ~3.1 K in monolayers. In addition, bulk material shows a broad kink around 30 K in $R(T)$ measurements, corresponding to the CDW transition. The CDW transition, however, is no longer visible for atomically thin samples due to possible broadening of the CDW feature [83].

3. Transport studies in BP

BP, which has relatively high hole mobility of 200 $cm^2\,V^{-1}\,s^{-1}$ at room temperature and a direct bandgap of 0.3 eV in bulk, and up to 2.0 eV in monolayer form [25–27], bridges the gap between zero bandgap graphene and large bandgap TMDs, making it an interesting addition to the existing 2D material family for nanoelectronics and nanophotonics applications [87–104]. BP is a stable phosphorus allotrope at room temperature [25, 26]. The structure of BP is formed from stacking puckered atomic layers which are held together by van der Waals interactions, much like graphite [105, 106]. These layers can be exfoliated and transferred onto different kinds of substrate [108, 109]. Single layer BP, known as phosphorene, have also been successfully mechanically exfoliated and its optical properties have been investigated [88, 99]. In this section, we broadly introduce electrical transport on BP in terms of its anisotropic transport properties and contact resistance. In addition to device perspective understanding, we also aim to cover the studies of low temperature magneto-transport on BP, including the Hall effect measurement, weak localization effect, as well as universal conductance fluctuation (UCF). More importantly, we would like to underscore the recent development of passivation techniques on BP, and provide an insightful path to fully explore the quantum phenomena of this 2D semiconductor.

3.1. Anisotropic transport in BP

Anisotropic transport was recorded in many early studies of BP [107, 110, 111], where the direction in the 2D plane perpendicular to the ridges shows the highest carrier mobility with the lowest effective mass. Recent density functional theory calculations have also demonstrated the values of effective mass. In the direction perpendicular to the ridges, known as the armchair direction, the effective mass of electrons and the hole is $m_e \approx m_h \approx 0.3\ m_0$. Along the direction parallel to the ridges, termed the zigzag direction, the effective mass of the hole is $m_h \approx 8.3\ m_0$, and the electron is $m_e \approx 2.6\ m_0$ [88, 103]. The crystal structure of BP is shown in figure 4(a). The unit cell contains eight atoms, which provides a calculated density of 2.69 g cm^{-3}. The anisotropic transport behavior along different directions can be electrically characterized. Detailed studies were carried out by Liu *et al* [88], in which a BP flake was peeled and transferred onto a 90 nm SiO_2 substrate, and metal contacts were symmetrically defined around the crystal in 45° increments. The maximum drain currents at a back gate voltage of −30 V, and drain voltage of −0.5 V were recorded and are displayed in figure 4(b) as a function of the orientation of the contact pair, showing a clear angle-dependent transport behavior. The anisotropic drain current revealed a roughly sinusoidal characteristic, where the maximum drain current occurs at 135 and 315° with a magnitude of 137 mA mm^{-1}, and a minimum drain current of 85 mA mm^{-1} happens at 45 and 225°. The same periodic trend can be simultaneously realized in the maximum value of transconductance, which could be partially related to an in-plane mobility variation. The significant difference in the drain current along different directions, together with the same periodic trend in mobility, provides strong evidence for anisotropic transport in BP. It has been shown experimentally by many groups that polarization-resolved Raman scattering could also examine the BP crystal orientation [89, 101, 112]. Three Raman peaks in thin film BP can be observed around 470, 440, and 365 cm^{-1}, corresponding to three A_g^2, B_{2g}, and A_g^1 vibration modes, respectively [113–116]. The peak positions do not change as the excitation light polarization varies; however, the relative intensity of these three peaks does change significantly with the polarization direction [101, 112, 113]. Indeed, the polarization-resolved Raman spectrum offers another method for determining the crystalline orientation of thin film BP, which is especially useful for relatively small flakes due to the small laser spot size.

3.2. Contact resistance of BP transistors

Another area of interest for BP is its device perspectives in terms of contact resistance [92]. An *I–V* output characteristic of a 3 μm channel length BP FET with an Ni contact is shown in figure 5(a). The on-state current increases as the gate bias changes from positive to negative voltage, which is a standard characteristic of a p-type transistor. The drain current varies linearly within the small drain bias regime, demonstrating an Ohmic-like contact resistance at the metal/BP interface with a small Schottky barrier height. An on-state drain current of 93.3 mA mm^{-1} for the 3 μm channel length in the Ni contact device is observed with $V_{bg} = -40$ V, and $V_{ds} = -2$ V. Using Pd contacts instead of Ni in a transistor on the same BP flake exhibits superior performance in terms of the on-state current, shown in figure 5(b). Examining the device with the same geometry as above, the Pd contact device has a drain current of 111.8 mA mm^{-1}. This larger on-state current of the Pd

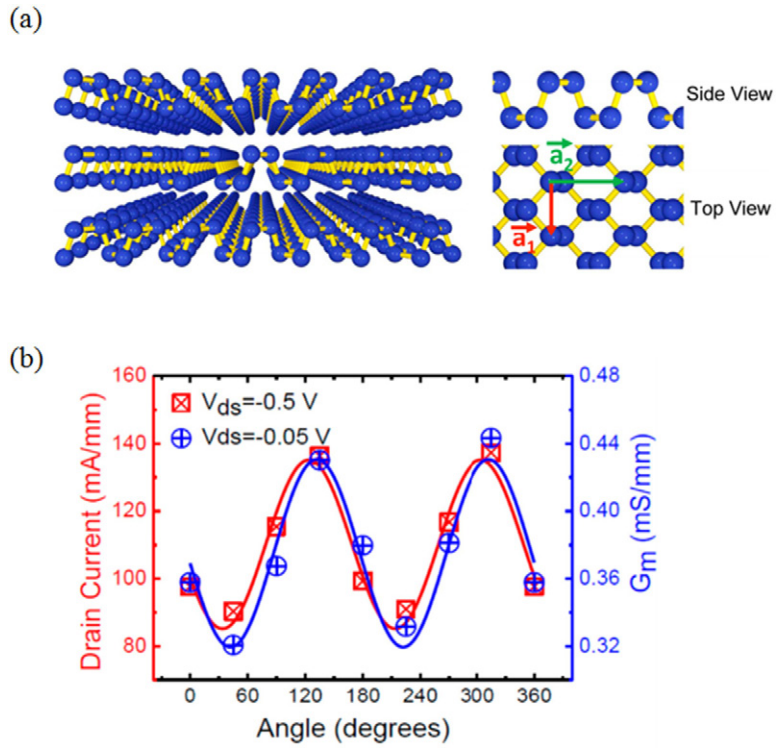

Figure 4. (a) Crystal structure and perspective side view of BP. (b) Angular dependence of the drain current and the transconductance G_m of a device. Reproduced with permission from [88]. Copyright 2014 American Chemical Society.

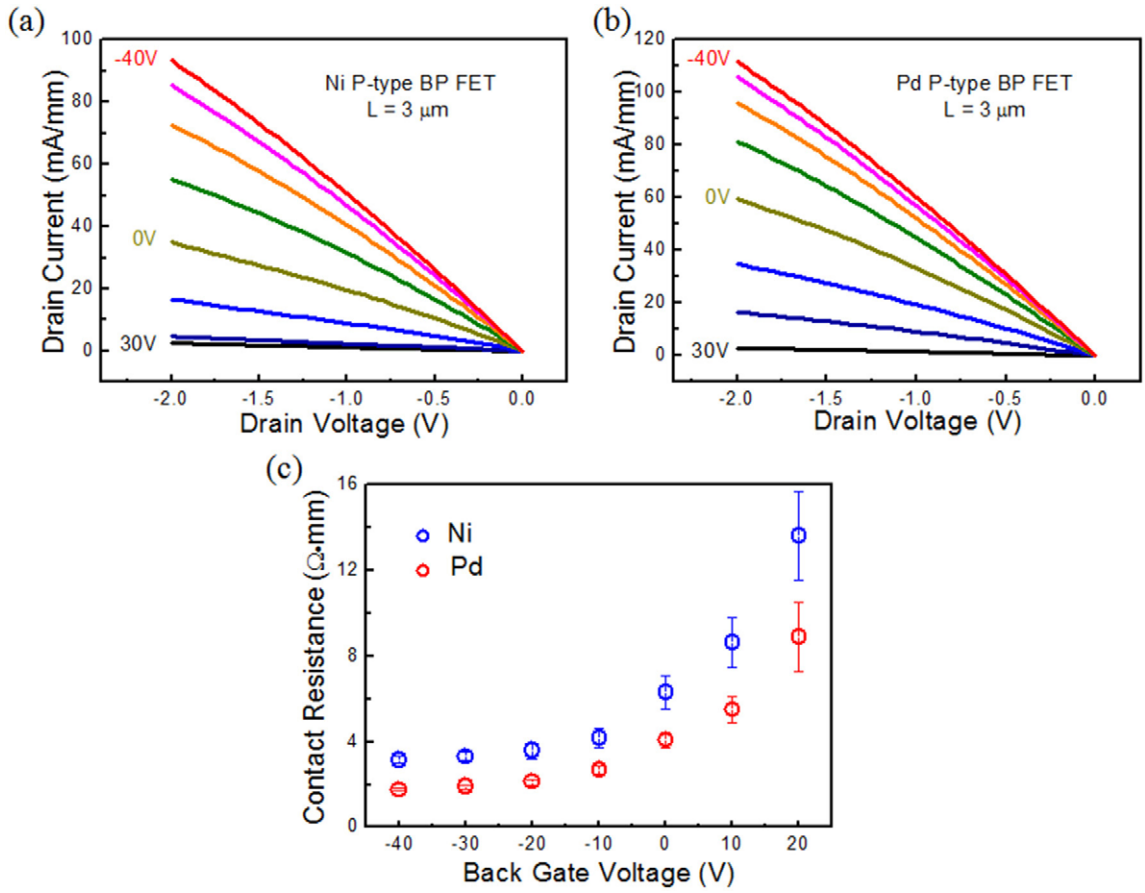

Figure 5. Output characteristic of a BP transistor with a channel length of 3 μm (a) Ni contact and (b) Pd contact. (c) Contact resistance for both Ni and Pd contact metals at various gate biases. Reproduced with permission from [92]. Copyright 2014 American Chemical Society.

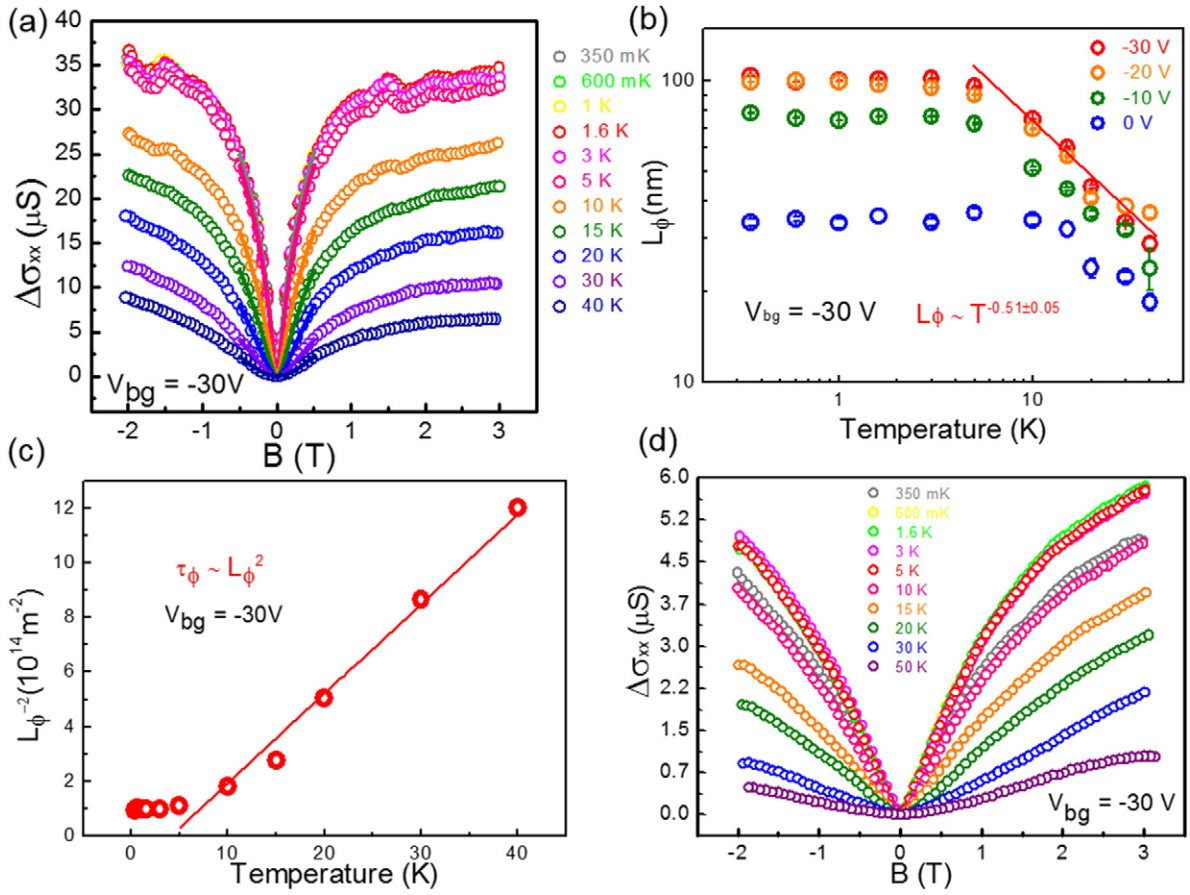

Figure 6. (a) Magneto-conductivity measurements of few-layer BP at a constant back gate bias of −30 V for various temperatures from the base temperature of 350 mK up to 40 K. (b) Phase coherence length varies with temperature at different back gate voltages. (c) Phase coherence length, L_ϕ^{-2} varies with different temperatures at a constant back gate voltage of −30 V. The phase coherence time is proportional to the L_ϕ^2, with a relation of $\tau_\phi \sim L_\phi^2$. (d) Magneto-conductivity measurements of few-layer phosphorene at a constant back gate bias of −30 V for various temperatures. Reproduced with permission from [122]. Copyright 2016 IOP Publishing Group.

transistor suggests that the Pd/BP contact has a smaller contact resistance compared to the Ni/BP contact. The transfer length method has been introduced and patterned on the same BP flake to determine the contact resistance of Ni/BP and Pd/BP. Referring to figure 5(c), the contact resistance of BP transistors shows a strong gate-dependent behavior, where the decrease of contact resistance at lower gate bias is related to the increase of electrostatically doped carrier density in BP under the metal contacts. The higher carrier density induced by the negative back gate voltage enhances the carrier concentration in the BP flake, which leads to a narrower Schottky barrier. Meanwhile, a narrowed Schottky barrier would thus facilitate the hole injection from the metal into the valence band of BP, lowering the contact resistance [117]. Figure 5(c) indicates that the contact resistance of Ni and Pd on the same BP flake saturates at around $3.15 \pm 0.15\ \Omega \cdot$ mm and $1.75 \pm 0.06\ \Omega \cdot$mm, respectively. This nearly 1.8 times reduction in contact resistance is mainly attributed to the different workfunction of the contact metals. The higher work-function metal Pd with 5.4 eV shows significantly smaller contact resistance than the 5.0 eV metal Ni, indicating that the Fermi-level aligned position of Pd is relatively closer to the valence band of BP. The contact resistance of metal/BP is much smaller compared to the intrinsic TMDs materials before applying localized doping techniques [117–121], which suggests a great potential for BP to be scaled down for high-speed transistors without the adverse effects related to dimensional scaling.

3.3. Thickness-dependent weak localization effect in BP

Magneto-conductivity measurements of weak localization on an 8.2 nm thick few-layer BP film with different temperatures are shown in figure 6(a) [122]. Similar to MoS_2, the strongly temperature-dependent weak localization effect in BP demonstrates a large dip at the base temperature of 350 mK, and quickly dies out as the temperature increases to 40 K. The weak localization effect is strongly gate-tunable, where the highly holey doped few-layer BP yields the largest correction to the magneto-conductivity at a back gate bias of −30 V. The maximum phase coherence length extracted from the low-B field portion by applying the HLN model is 104 nm at 350 mK and −30 V back gate bias. As the temperature increases from 5 K up to 40 K, the phase coherence length demonstrates a power-law behavior of $\sim T^{-\gamma}$, shown in figure 6(b). At a constant of −30 V back gate bias, the phase coherence length decays with temperature as $\sim T^{-0.513\pm0.05}$ over the studied

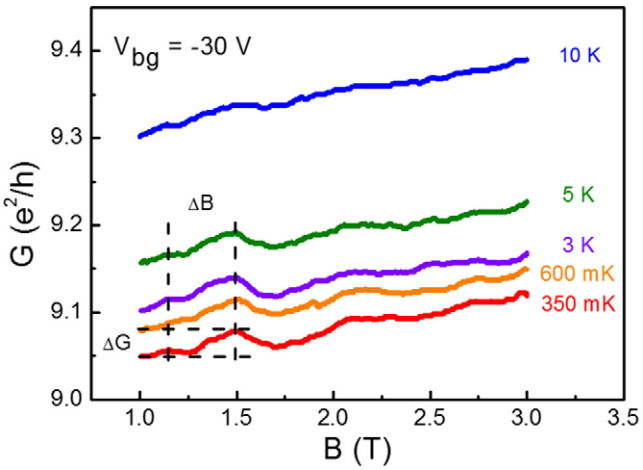

Figure 7. Magneto-conductance fluctuation in a few-layer BP sample for a range of studied temperatures. Reproduced with permission from [122]. Copyright 2016 IOP Publishing Group.

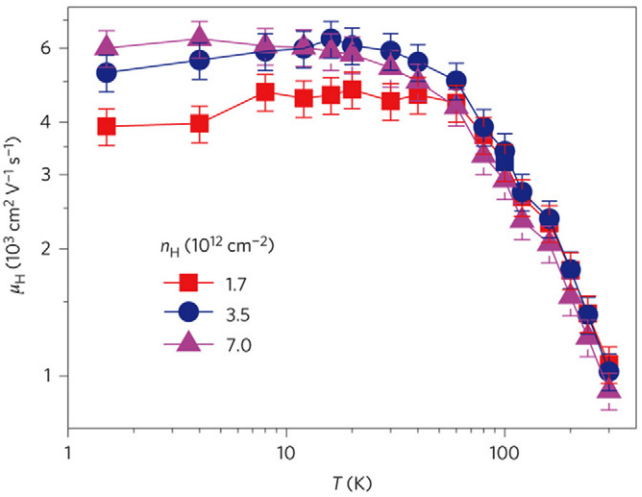

Figure 8. Hall mobility as a function of temperature measured at varying hole carrier densities. Reproduced with permission from [132]. Copyright 2016 Nature Publishing Group.

temperature range, which matches the observation from previous studies that hole–hole scattering would give an exponent of −0.5 in a 2D system [32, 35]. The phase coherence length is related to the phase coherence time by the diffusion coefficient as $L_\phi = \sqrt{D\tau_\phi}$, where τ_ϕ is the phase coherence time, and D is the diffusion coefficient. Meanwhile, the diffusion coefficient is found from the relation $D = \frac{\sigma}{e^2 g_{2D}(E_F)} = \frac{\sigma\pi\hbar^2}{m^* e^2}$ where σ is the conductivity in the channel, and m^* the effective mass of carriers in the few-layer BP. Instead of calculating the exact value of phase coherence time, quantitative behavior analysis of phase coherence time can be realized. Phase coherence length, L_ϕ^{-2}, which is directly proportional to phase coherence time τ_ϕ^{-1} is plotted in figure 6(c) as a function of temperature. The linear dependence between phase coherence time and temperature agrees well with the prediction of the theory of carrier interaction in the diffusive regime, showing a conventional behavior of carrier interference [123, 124]. Thickness-dependent weak localization has also been studied, in which a few-layer phosphorene film with a thickness of 4.5 nm has been probed. A strong temperature-dependent weak localization effect is given in figure 6(d), where the shape of differential magneto-conductivity is similar to a few-layer BP sample, but with a greatly reduced magnitude due to a smaller carrier mobility. The phase coherence length which varies with different temperatures has been unfolded, and the largest phase coherence length in a few-layer phosphorene sample is 49.1 nm at 600 mK, which is much smaller compared to the one in the few-layer BP at the same condition. The reduction of the phase coherence length is also a result of decreased mobility for thinner BP film which enters HLN theory as a decreased diffusion coefficient, where $D = \frac{\sigma\pi\hbar^2}{m^* e^2}$ allows the diffusion coefficient to be calculated from the conductivity.

3.4. UCF effect in BP

UCF is a quantum interference effect of diffusive charge carriers, observed commonly in semiconductors, metals, and graphene [125, 126]. The mesoscopic nature or finite size of a weakly disordered sample results in the loss of the self-averaging of its physical properties. Application of a magnetic field to semiconductors varies the phase of the wave function of charge carriers, where the magnitude and interval of conductance fluctuation are closely related to the phase coherence length [126]. The UCF effect is realized in few-layer BP samples under high magnetic fields and at low temperatures [122]. Figure 7 illustrates magneto-conductance traces in an order of e^2/h change at different temperatures. The UCF effect in BP is very sensitive to temperature, where the fluctuation remains consistent at low temperatures from 350 mK up to 5 K; however, it decays quickly as the temperature increases above 10 K. The characteristic interval for magneto-conductance fluctuation ΔB, with a magnitude of 0.38 T for the few-layer BP at a base temperature of 350 mK, is robust, and persists to temperatures as high as 5 K. Also, the amplitude of magneto-conductance fluctuation, ΔG, is 0.027 e^2/h at $T = 350$ mK for a few-layer sample, and maintains almost the same value between 350 mK and 5 K. It is clear that both the magnitude and interval of conductance fluctuation die out rapidly as the temperature increases, consistent with the idea that phase coherence length decays with temperature, indicating that the magnitude and interval of conductance fluctuation are closely related to the phase coherence length. The UCF effect has also been examined in a few-layer phosphorene sample; however, no obvious fluctuations have been observed within the studied ranges of temperature and magnetic field, which is attributed to the decreased phase coherence length.

3.5. Passivation techniques in BP

Many layered materials can be exfoliated from bulk down to one single atomic layer, but only a small number of them are stable under an ambient atmosphere. The reduced chemical stability of 2D materials is associated with the energy needed to maintain stable bonding configurations, which is affected by electrostatics and structural buckling

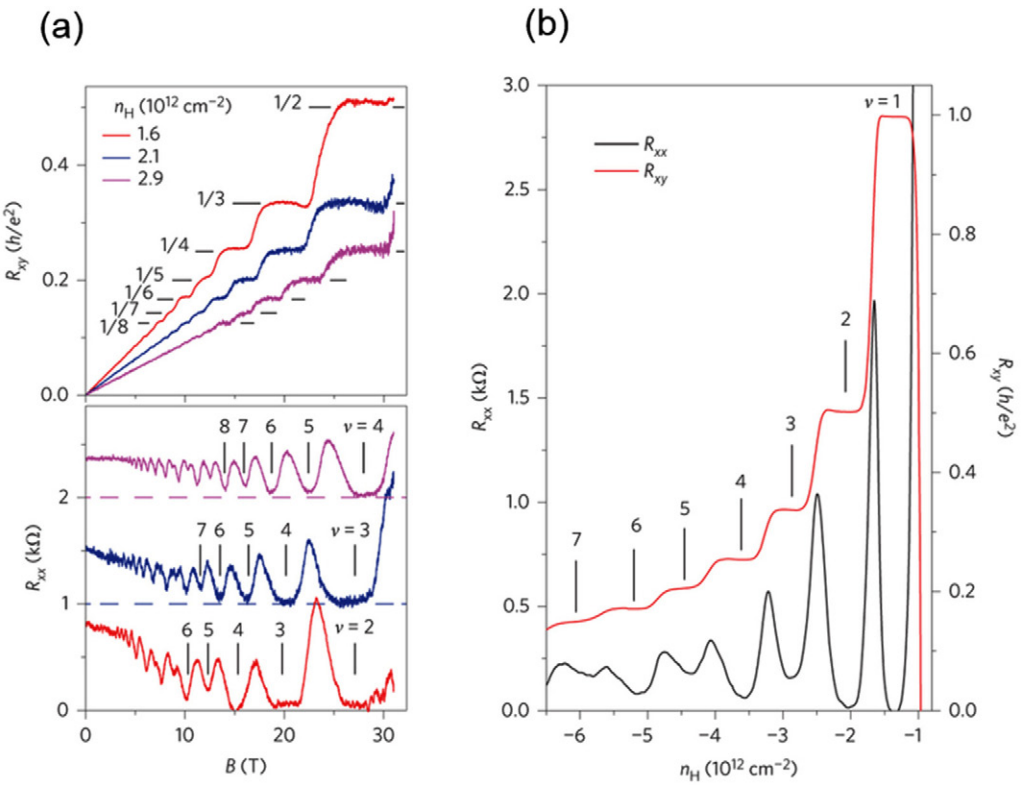

Figure 9. (a) Hall resistance (upper panel) and magneto-resistance (lower panel) as a function of magnetic field measured at varying hole doping levels. (b) Hall resistance (black) and magneto-resistance (red) as a function of gate voltage. Data were obtained at $B = 31$ T and $T = 300$ mK. Integers indicate the filling factor ν at each quantum state. Quantum plateaus are observed at ν from 1 to 7. Reproduced with permission from [132]. Copyright 2016 Nature Publishing Group.

[127–129]. Thus, ambient stability is likely to be a concern for few-layer phosphorene since phosphorus atoms have free lone pairs and valence bond angles of 102° within the lattice [128, 133]. Surface instability has been observed in several studies regarding the isolation of thin layers of BP [90, 91], but the mechanism of surface degradation is not well understood. Researchers have suggested that O_2 saturated H_2O irreversibly reacts with BP to form an oxidized phosphorus species, at a significant cost to electronic characteristics [127, 128]. Certain passivation techniques have recently been proposed, such as atomic layer deposited Al_xO_y [95, 107, 128], hydrophobic polymers [130, 131], and multi-layer hBN [132–138]. Through effective passivation, BP transistors can sustain good electrical performance for weeks and months. Li *et al* recently achieved an enhanced Hall mobility in BP at low temperatures [132], which is much higher than previous recorded values. The device is accomplished by constructing a van der Waals heterostructure with few-layer BP sandwiched between two hBN flakes, and placed on a graphite back gate. The top hBN only protects the BP flake from degradation in air, but also further prevents surface scattering from neighboring adsorbates. Additionally, the bottom hBN layer allows the electrons in the graphite to screen the impurity potential at the BP/hBN interface, where the impurities at the interface are mainly responsible for the limited low-temperature Hall mobility of BP. High quality hBN-encapsulated BP has brought the carrier Hall mobility up to 6000 cm^2 V^{-1} s^{-1} at low temperature. Mobility characterization of BP is shown in figure 8, which demonstrates Hall mobility as a function of temperature measured at varying hole carrier densities. For all carrier densities, Hall mobility increases with decreasing temperature and starts to saturate at 30 K. The low-temperature mobility is much higher than previously reported values, and has a typical temperature-dependent semiconductor behavior. It suggests that the charge transport is dominated by electron–phonon scattering at temperature regimes above 30 K, and can be characterized by a $T^{-1/2}$ relation. The low-temperature mobility has a much reduced influence from charge impurities as a result of the protection provided by the hBN encapsulation.

3.6. Quantum phenomenon in a hBN-encapsulated BP heterostructure

The high mobility of the hBN heterostructure sample is further corroborated by probing the SdH oscillations as reported by Li *et al* [132]. The oscillations start from a critical magnetic field of $B_c = 2$ T. An independent estimation of the carrier mobility $\mu \sim 1/B_c$ therefore puts the mobility at ~5000 cm^2 V^{-1} s^{-1}. The estimation agrees with the mobility obtained from the Hall effect measurements, which further evidences the high quality of the hBN-encapsulated heterostructure device. The exceptional carrier mobility enables an observation of the QHE for the first time in BP. Figure 9(a) shows the magneto-resistance (R_{xx}) and Hall resistance (R_{xy}) as a function of the applied magnetic field at varying carrier densities. At high magnetic field, the Hall resistance exhibits quantized plateaus, together with a vanishing longitude resistance, which are the hallmarks

of QHE. The plateaus are defined at $\nu = 1$, 2, 3, and 4, and developing plateaus are observed up to $\nu = 8$. R_{xx} and R_{xy} measured as a function of V_g with magnetic field fixed at $B = 31$ T is shown in figure 9(b). The results show that the lowest Landau level has been approached, and the transport study is towards the extreme quantum limit. The quantum states developed in BP have shown both odd and even integers, indicating that the two-fold spin degeneracy in BP is fully lifted.

4. Conclusion

The emerging field of 2D materials from gapless graphene, and narrow bandgap BP, to wide bandgap TMDs, has never ceased to surprise due to their unique crystal structures and fundamental properties. The rise of 2D materials has provided the condensed-matter field with a brand new class of materials that are atomically thin, and has offered many opportunities to study new physical phenomena which are unobservable in 3D bulk structures. The progenitor of this family, graphene, has enjoyed many advantages, and no longer requires any further proof of its importance. Apart from its limitations in logic electronics, graphene has already offered many scientific discoveries across transport studies. On the other hand, despite currently being extensively studied due to the their reasonable band gap structures, the carrier mobility of TMDs have so far been substantially below the theoretically predicted limits, which has severely hindered investigations into their quantum transport behaviors. Fortunately, a van der Waals heterostructure platform has provided a practical path, moving forward, to achieve improved mobility by reducing the interfacial impurities and phonon scattering. This has enabled the first observation of SdH oscillations in MoS_2, and may become an effective tool to access low-temperature quantum phenomenon in other TMD materials. BP, a recently rediscovered layered material with a much higher carrier mobility, is a semiconductor with a bandgap which ranges from 0.3 eV in bulk material to 2.0 eV for monolayer phosphorene. Additionally, BP demonstrates anisotropic transport and superconductivity under high pressure. A relatively high intrinsic carrier mobility together with hBN-encapsulation techniques have allowed BP to exhibit an exceptionally high hole mobility at low temperatures and set the stage for realizing integer QHE. We presented here a short overview on the transport studies in TMDs and BP, and we sincerely hope it will help to inspire more exciting discoveries in this growing 2D materials field. Certainly many challenging problems still remain, requiring further developments to overcome them. With continuous efforts in consummating material properties, our society may benefit from 2D-materials-based functional devices in the near future.

Acknowledgments

The authors thank T Murphy, J-H Park, and G Jones for their technical support at the National High Magnetic Field Laboratory (NHMFL). This material is based upon work supported by NSF under Grant ECCS-1449270, AFOSR/NSF under EFRI 2-DARE Grant EFMA-1433459, and ARO under Gant W911NF-14-1-0572.

References

[1] Geim A K and Novoselov K S 2007 *Nat. Mater.* **6** 183–91
[2] Novoselov K S, Falko V I, Colombo L, Gellert P R, Schwab M G and Kim K 2012 *Nature* **490** 192–200
[3] Novoselov K S, Geim A K, Morozov S, Jiang D, Katsnelson M, Grigorieva I, Dubonos S V and Firsov A 2005 *Nature* **438** 197–200
[4] Geim A K 2009 *Science* **324** 1530–34
[5] Du X, Skachko I, Barker A and Andrei E Y 2008 *Nat. Nanotechnol.* **3** 491–5
[6] Zhang Y, Tan Y W, Stormer H L and Kim P 2005 *Nature* **438** 201–4
[7] Schwierz F 2010 *Nat. Nanotechnol.* **5** 487–96
[8] Neto A C, Guinea F, Peres N, Novoselov K S and Geim A K 2009 *Rev. Mod. Phys.* **81** 109
[9] Han M Y, Oezyilmaz B, Zhang Y and Kim P 2007 *Phys. Rev. Lett.* **98** 206805
[10] Wu Y, Lin Y M, Bol A A, Jenkins K A, Xia F, Farmer D B, Zhu Y and Avouris P 2011 *Nature* **472** 74–8
[11] Jariwala D, Srivastava A and Ajayan P M 2011 *J. Nanosci. Nanotechnol.* **11** 6621–41
[12] Zhang H, Bekyarova E, Huang J W, Zhao Z, Bao W, Wang F, Haddon R C and Lau C N 2011 *Nano Lett.* **11** 4047–51
[13] Farmer D B, Chiu H Y, Lin Y M, Jenkins K A, Xia F and Avouris P 2009 *Nano Lett.* **9** 4474–78
[14] Chhowalla M, Shin H S, Eda G, Li L J, Loh K P and Zhang H 2013 *Nat. Chem.* **5** 263–75
[15] Jariwala D, Sangwan V K, Lauhon L J, Marks T J and Hersam M C 2014 *ACS Nano* **8** 1102–20
[16] Radisavljevic B, Radenovic A, Brivio J, Giacometti V and Kis A 2011 *Nat. Nanotechnol.* **6** 147–50
[17] Mak K F, Lee C, Hong J, Shan J and Heinz T F 2010 *Phys. Rev. Lett.* **105** 136805
[18] Liu H and Ye P D 2011 *IEEE Electron Device Lett.* **33** 546–8
[19] Liu H, Gu J J and Ye P D 2012 *IEEE Electron Device Lett.* **33** 1273–5
[20] Liu H, Si M, Najmaei S, Neal A T, Du Y, Ajayan P M, Lou J and Ye P D 2013 *Nano Lett.* **13** 2640–6
[21] Wang H, Yu L, Lee Y H, Shi Y, Hsu A, Chin M L, Li L J, Dubey M, Kong J and Palacios T 2012 *Nano Lett.* **12** 4674–80
[22] Radisavljevic B, Whitwick M B and Kis A 2011 *ACS Nano* **5** 9934–8
[23] Yoon Y, Ganapathi K and Salahuddin S 2011 *Nano Lett.* **11** 3768–73
[24] Fang H, Chuang S, Chang T C, Takei K, Takahashi T and Javey A 2012 *Nano Lett.* **12** 3788–92
[25] Warschauer D 1963 *J. Appl. Phys.* **34** 1853–60
[26] Nishii T, Maruyama Y, Inabe T and Shirotani I 1987 *Synth. Met.* **18** 559–64
[27] Narita S 1983 *Phys. Soc. Japan* **52** 2148–55
[28] Bridgman P B 1914 *J. Am. Chem. Soc.* **36** 1344–63
[29] Kang J, Tongay S, Zhou J, Li J and Wu J 2013 *Appl. Phys. Lett.* **102** 012111
[30] Splendiani A, Sun L, Zhang Y, Li T, Kim J, Chim C Y, Galli G and Wang F 2010 *Nano Lett.* **10** 1271–5
[31] Wu S, Huang C, Aivazian G, Ross J S, Cobden D H and Xu X 2013 *ACS Nano* **7** 2768–72
[32] Neal A T, Liu H, Gu J J and Ye P D 2013 *ACS Nano* **7** 7077–82
[33] Likovich E M, Russell K J, Petersen E W and Narayanamurti V 2009 *Phys. Rev.* B **80** 245318
[34] Hikami S, Larkin A I and Nagaoka Y 1980 *Prog. Theor. Phys.* **63** 707–10
[35] Altshuler B L and Aronov A G 1985 *Electron–Electron Interaction in Disordered Systems* (North Holland: Elsevier)
[36] Li X, Mullen J T, Jin Z, Borysenko K M, Nardelli M B and Kim K W 2013 *Phys. Rev.* B **87** 115418

[37] Kaasbjerg K, Thygesen K and Jacobsen K 2012 *Phys. Rev.* B **85** 115317
[38] Ma N and Jena D 2014 *Phys. Rev. X* **4** 011043
[39] Liu K K *et al* 2012 *Nano Lett.* **12** 1538–44
[40] Zhan Y, Liu Z, Najmaei S, Ajayan P M and Lou J 2012 *Small* **8** 966–71
[41] Lee Y H *et al* 2012 *Adv. Mater.* **24** 2320–5
[42] Najmaei S, Liu Z, Zhou W, Zou X, Shi G, Lei S, Yakobson B I, Idrobo J C, Ajayan P M and Lou J 2013 *Nat. Mater.* **12** 754–9
[43] Liu D, Guo Y, Fang L and Robertson J 2013 *Appl. Phys. Lett.* **103** 183113
[44] Late D J *et al* 2013 *ACS Nano* **7** 4879–91
[45] Qiu H, Pan L, Yao Z, Li J, Shi Y and Wang X 2012 *Appl. Phys. Lett.* **100** 123104
[46] Radisavljevic B and Kis A 2013 *Nat. Mater.* **12** 815–20
[47] Cui X *et al* 2015 *Nat. Nanotechnol.* **10** 534–40
[48] Eda G, Fujita T, Yamaguchi H, Voiry D, Chen M and Chhowalla M 2012 *ACS Nano* **6** 7311–7
[49] Lee S and Zhong Z 2014 *Nanoscale* **6** 13283–330
[50] Joensen P, Frindt R F and Morrison S R 1986 *Mater. Res. Bull.* **21** 457–61
[51] Yang D and Frindt R F 1996 *J. Phys. Chem. Solids* **57** 1113–6
[52] Py M A and Haering R R 1983 *Can. J. Phys.* **61** 76–84
[53] Neto A H C 2001 *Phys. Rev. Lett.* **86** 4382
[54] Kappera R, Voiry D, Yalcin S E, Branch B, Gupta G, Mohite A D and Chhowalla M 2014 *Nat. Mater.* **13** 1128–34
[55] Hulliger F 1968 *Struct. Bonding* **4** 83–229
[56] Wilson J and Yoffe A 1969 *Adv. Phys.* **18** 193–335
[57] Wilson J, Di Salvo F and Mahajan S 1975 *Adv. Phys.* **24** 117–201
[58] Ritschel T, Trinckauf J, Garbarion G, Hanfland M, Zimmermann M V, Berger H, Buchner B and Geck J 2013 *Phys. Rev.* B **87** 125135
[59] Yu Y *et al* 2015 *Nat. Nanotechnol.* **10** 270–6
[60] Neal A T, Du Y, Liu H and Ye P D 2014 *ACS Nano* **8** 9137–42
[61] Rossnagel K and Smith N V 2007 *Phys. Rev.* B **76** 073102
[62] Ueno K, Nakamura S, Shimotani H, Ohtomo A, Kimura N, Nojima T, Aoki H, Iwasa Y and Kawasaki M 2008 *Nat. Mater.* **7** 855–8
[63] Ye J T, Inoue S, Kobayashi K, Kasahara Y, Yuan H T, Shimotani H and Iwasa Y 2010 *Nat. Mater.* **9** 125–8
[64] Ueno K, Nakamura S, Shimotani H, Yuan H T, Kimura N, Nojima T, Aoki H, Iwasa Y and Kawasaki M 2011 *Nat. Nanotechnol.* **6** 408–12
[65] Yuan H *et al* 2013 *Nat. Phys.* **9** 563–9
[66] Shibata K, Yuan H, Iwasa Y and Hirakawa K 2013 *Nat. Commun.* **4** 2664
[67] Zhang Y J, Ye J T, Yomogida Y, Takenobu T and Iwasa Y 2013 *Nano Lett.* **13** 3023–8
[68] Lu J M, Zheliuk O, Leermakers I, Yuan N F Q, Zeitler U, Law K T and Ye J T 2015 *Science* **350** 1353–7
[69] Zhang Y, Ye J T, Matsuhashi Y and Iwasa Y 2012 *Nano Lett.* **12** 1136–40
[70] Bollinger A T, Dubuis G, Yoon J, Pavuna D, Misewich J and Bozovic I 2011 *Nature* **472** 458–60
[71] Leng X, Garcia-Barriocanal J, Bose S, Lee Y and Goldman A M 2011 *Phys. Rev. Lett.* **107** 027001
[72] Ye J T, Zhang Y J, Akashi R, Bahramy M S, Arita R and Iwasa Y 2012 *Science* **338** 1193–6
[73] Taniguchi K, Matsumoto A, Shimotani H and Tkagi H 2012 *Appl. Phys. Lett.* **101** 042603
[74] Jo S, Costanzo D, Berger H and Morpurgo A F 2015 *Nano Lett.* **15** 1197–202
[75] Hromadova L, Martonak R and Tosatti E 2013 *Phys. Rev.* B **87** 144105
[76] Riflikova M, Martonak R and Tosatti E 2014 *Phys. Rev.* B **90** 035108
[77] Nayak A P, Bhattacharyya S, Zhu J, Liu J, Wu X, Pandey T, Jin C, Singh A K, Akinwande D and Lin J F 2014 *Nat. Commun.* **5** 3731
[78] Chi Z H, Zhao X M, Zhang H, Goncharov A F, Lobanov S S, Kagayama T, Sakata M and Chen X J 2014 *Phys. Rev. Lett.* **113** 036802
[79] Livneh T and Sterer E 2010 *Phys. Rev.* B **81** 195209
[80] Chi Z H *et al* 2015 arXiv:1503.05331
[81] Pan X C *et al* 2015 *Nat. Commun.* **6** 7805
[82] Frindt R F 1972 *Phys. Rev. Lett.* **28** 299
[83] Xi X, Zhao L, Wang Z, Berger H, Forro L, Shan J and Mak K F 2015 *Nat. Nanotechnol.* **10** 765–9
[84] Staley N E, Wu J, Eklund P and Liu Y 2009 *Phys. Rev.* B **80** 184505
[85] Xi X, Wang Z, Zhao W, Park J-H, Law K T, Berger H, Forro L, Shan J and Mak K F 2016 *Nat. Phys.* **12** 139–43
[86] Ugeda M M *et al* 2016 *Nat. Phys.* **12** 92–7
[87] Li L, Yu Y, Ye G J, Ge Q, Ou X, Wu H, Feng D, Chen X H and Zhang Y 2014 *Nat. Nanotechnol.* **9** 372–7
[88] Liu H, Neal A T, Zhu Z, Luo Z, Xu X, Tomanek D and Ye P D 2014 *ACS Nano* **8** 4033–41
[89] Xia F, Wang H and Jia Y 2014 *Nat. Commun.* **5** 4458
[90] Gomez A *et al* 2014 *2D Mater.* **1** 025001
[91] Koenig S P, Doganov R A, Schmidt H, Neto A H C and Ozyilmaz B 2014 *Appl. Phys. Lett.* **104** 103106
[92] Du Y, Liu H, Deng Y and Ye P D 2014 *ACS Nano* **8** 10035–42
[93] Haratipour N, Robbins M C and Koester S J 2014 *IEEE Electron Device Lett.* **36** 411–3
[94] Das S, Demarteau M and Roelofs A 2014 *ACS Nano* **8** 11730–8
[95] Liu H, Neal A T, Si M, Du Y and Ye P D 2014 *IEEE Electron Device Lett.* **35** 795–7
[96] Wang H, Wang X, Xia F, Wang L, Jiang H, Xia Q, Chin M L, Dubey M and Han S J 2014 *Nano Lett.* **14** 6424–9
[97] Du Y, Yang L, Zhou H and Ye P D 2016 *IEEE Electron Device Lett.* **37** 429–32
[98] Buscema M, Groenendijk D J, Blanter S I, Steele G A, Zant H S J and Castellanos-Gomez A 2014 *Nano Lett.* **16** 3347–52
[99] Wang X, Jones A M, Seyler K L, Tran V, Jia Y, Zhao H, Wang H, Yang L, Xu X and Xia F 2015 *Nat. Nanotechnol.* **10** 517–21
[100] Deng Y, Luo Z, Conrad N J, Liu H, Gong Y, Najmaei S, Ajayan P M, Lou J, Xu X and Ye P D 2014 *ACS Nano* **8** 8292–9
[101] Luo Z, Maassen J, Deng Y, Du Y, Lundstrom M S, Ye P D and Xu X 2015 *Nat. Commun.* **6** 8572
[102] Youngblood N, Chen C, Koester S J and Li M 2015 *Nat. Photo.* 2015
[103] Liu H, Du Y, Deng Y and Ye P D 2015 *Chem. Soc. Rev.* **44** 2732–43
[104] Xiang Z *et al* 2015 *Phys. Rev. Lett.* **115** 186403
[105] Jiang J-W and Park H S 2014 *Nat. Commun.* **5** 4727
[106] Rodin A S, Carvalho A and Castro Neto A H 2014 *Phys. Rev. Lett.* **112** 176801
[107] Luo X, Rahbarihagh Y, Hwang J, Liu H, Du Y and Ye P D 2014 *IEEE Electron Device Lett.* **35** 1314–6
[108] Baba M, Nakamura Y, Takeda Y, Shibata K, Morita A, Koike Y and Fukase T 1992 *J. Phys.: Condens. Matter* **4** 1535–44
[109] Maruyama Y, Suzuki S, Kobayashi K and Tanuma S 1981 *Physica* **105** 99–102
[110] Shirotani I 1982 *Mol. Cryst. Liq. Cryst.* **86** 203–11
[111] Akahama Y, Endo S and Narita S 1986 *Physica* **139** 397–400
[112] Wu J, Mao N, Xie L, Xu H and Zhang J 2015 *Angew. Chem.* **127** 2396–9
[113] Ling X, Liang L, Huang S, Puretzky A A, Geohegan D B, Sumpter B G, Kong J, Meunier V and Dresselhaus M S 2015 *Nano Lett.* **15** 4080–8

[114] Feng Y, Zhou J, Du Y, Miao F, Duan C G, Wang B and Wan X 2015 *J. Phys.: Condens. Matter* **27** 185302
[115] Manjanath A, Samanta A, Pandey T and Singh A K 2015 *Nanotechnology* **26** 075701
[116] Fei R and Yang L 2014 *Appl. Phys. Lett.* **105** 083120
[117] Du Y, Yang L, Liu H and Ye P D 2014 *APL Mater.* **2** 092510
[118] Du Y, Liu H, Neal A T, Si M and Ye P D 2013 *IEEE Electron Device Lett.* **34** 1328–30
[119] Das S, Chen H Y, Penumatcha A V and Appenzeller J 2013 *Nano Lett.* **13** 100–5
[120] Du Y, Yang L, Zhang J, Liu H, Majumdar K, Kirsch P D and Ye P D 2014 *IEEE Electron Device Lett.* **35** 599–601
[121] Yang L *et al* 2014 *Nano Lett.* **14** 6275–80
[122] Du Y, Neal A T, Zhou H and Ye P D 2016 *2D Mater.* **3** 024003
[123] Tikhonenko F V, Horsell D W, Gorbachev R V and Savchenko A K 2008 *Phys. Rev. Lett.* **100** 056802
[124] Gorbachev R V, Tikhonenko F V, Mayorov A S, Horsell D W and Savchenko A K 2007 *Phys. Rev. Lett.* **98** 176805
[125] Morozov S V, Novoselov K S, Katsnelson M I, Schedin F, Ponomarenko L A, Jiang D and Geim A K 2006 *Phys. Rev. Lett.* **97** 016801
[126] Staley N E, Puls C P and Liu Y 2008 *Phys. Rev.* B **77** 155429
[127] Favron A, Gaufres E, Fossard F, Phaneuf-L'Heureux A, Tang N Y-W, Levesque P L, Loiseau A, Leonelli R, Francoeur S and Martel R 2015 *Nat. Mater.* **14** 826–32
[128] Wood J D, Wells S A, Jariwala D, Chen K S, Cho E, Sangwan V K, Liu X, Lauhon L J, Marks T J and Hersam M C 2014 *Nano Lett.* **14** 6964–70
[129] Molle A, Grazianetti C, Chiappe D, Cinquanta E, Cianci E, Tallarida G and Fanciulli M 2013 *Adv. Funct. Mater.* **23** 4340–4
[130] Mu H *et al* 2015 *Adv. Opt. Mater.* **3** 1447–53
[131] Kim J S, Liu Y, Zhu W, Kim S, Wu D, Tao Li, Dodabalapur A, Lai K and Akinwande D 2015 *Sci. Rep.* **5** 8989–95
[132] Li L *et al* 2016 *Nat. Nanotechnol.* (DOI:10.1038/nnano.2016.42)
[133] Li L *et al* 2015 *Nat. Nanotechnol.* **10** 608–13
[134] Gillgren N *et al* 2015 *2D Mater.* **2** 011001
[135] Chen X *et al* 2015 *Nat. Commun.* **6** 7315
[136] Cao Y *et al* 2015 *Nano Lett.* **15** 4914–21
[137] Doganov R A *et al* 2015 *Nat. Commun.* **6** 6647
[138] Avsar A, Vera-Marun I J, Tan J Y, Watanabe K, Taniguchi T, Neto A H C and Ozyilmaz B 2015 *ACS Nano* **9** 4138–45